water

MDPI

Article

Scour Development Around an Oblong Bridge Pier: A Numerical and Experimental Study

Ana Margarida Bento [1,2,*], João Pedro Pêgo [1,2], Teresa Viseu [3] and Lúcia Couto [3]

[1] Hydraulics, Water Resources and Environmental Division, Civil Engineering Department, Faculty of Engineering, University of Porto, 4400-465 Porto, Portugal; jppego@fe.up.pt
[2] Interdisciplinary Centre of Marine and Environmental Research, 4450-208 Matosinhos, Portugal
[3] Water Resources and Hydraulic Structures Division, Hydraulics and Environment Department, National Laboratory of Civil Engineering, 1700-066 Lisboa, Portugal; tviseu@lnec.pt (T.V.); luciacoutoribeiro@gmail.com (L.C.)
* Correspondence: anabento@fe.up.pt

Abstract: The complex flow structure around bridge piers is challenging for both experimental and numerical studies. Therefore, investigating the capabilities of Computational Fluid Dynamics (CFD) tools in resolving the flow structure and the mechanism of sediment entrainment into and out of the scour hole remains a challenging task. In this study, the scour depth around an oblong bridge pier and the bed shear stress distributions in time and space were numerically investigated using the Computational Fluid Dynamics (CFD) tool Sediment Simulation In Intakes with Multiblock option (SSIIM). Clear water scour conditions and sand of known granulometric composition were considered in accordance with the experimental study carried out. Laboratory data and the results of a scour characterization around a 0.11 m wide oblong bridge pier were considered to calibrate and validate the numerical model. The averaged form of the Navier–Stokes equations was considered to simulate the turbulent flow fields in anticipation of long time scales. The results show that calibrated numerical models can reproduce measured scour depths in the laboratory environment with considerable accuracy, with an average relative error of less than 3%, especially around oblong bridge piers.

Keywords: bed shear stress; bridge pier; sediment transport; scour hole; SSIIM software

Citation: Bento, A.M.; Pêgo, J.P.; Viseu, T.; Couto, L. Scour Development Around an Oblong Bridge Pier: A Numerical and Experimental Study. *Water* **2022**, *15*, 2867. https://doi.org/10.3390/w15162867

Academic Editor: Roberto Gaudio

Received: 1 July 2023
Revised: 31 July 2023
Accepted: 7 August 2023
Published: 8 August 2023

1. Introduction

The local scour phenomenon has been recognised for decades as a serious threat to the stability of bridges worldwide [1–3]. In Portugal, the tragic accident at the Hintze-Ribeiro bridge on the Douro River was partly due to erosion around one of its foundations [4]. This phenomenon results from the dynamic interactions between the three-dimensional turbulent flow field and the mobile riverbed in the vicinity of the bridge foundations, which are amplified during the development of a scour hole. Due to the involvement of several complex mechanisms, mainly of a hydraulic nature, the scour process has remained a challenging engineering problem for many decades [5].

Numerous experimental and numerical studies have attempted to resolve the flow structure and the mechanism of sediment entrainment into and out of the scour hole, mostly for piers with a circular cross-section geometry. Dargahi [6] was a pioneer in the experimental investigation of flow patterns, turbulence intensity and boundary shear stress distributions in the scour zone of a circular pier. The study was carried out for different fixed scour stages under clear water conditions. Based on these results, several other experimental studies have been carried out to investigate the flow mechanism and the associated scour process around single piers [7–13], among others.

After decades of research on experimental controlled environments, fewer works have devoted their attention to the three-dimensional numerical simulation of these processes.

Nevertheless, some first steps have been taken to achieve a numerical characterisation of the flow patterns [14] in order to accurately complement the experimental efforts. For a laminar steady horseshoe vortex at the intersection of an elliptical strut and a flat plate, Briley and McDonald [15] carried out numerical solutions of the compressible Navier–Stokes equations, while Kwak et al. [16] computed the laminar steady junction flow by means of a three-dimensional incompressible Navier–Stokes code. However, when the flow is turbulent, the computational prediction of the separation flow is a process of critical importance as it significantly influences the numerical performance in reproducing the physical phenomenon. The fluctuation of turbulent flows on a wide range of time and length scales makes their numerical computation difficult and requires a specific way of modelling this turbulence. The Reynolds-Averaged Navier–Stokes (RANS) equations are such model equations, and were used in the first application of Computational Fluid Dynamic (CFD) tools by Deng and Piquet [17], to study the three-dimensional turbulent flow around an airfoil. The use of an iterative, fully decoupled technique to compute the RANS equations proved to be an attractive approach to capture the main features of horseshoe vortices, although they lacked some accuracy in modelling the scouring process. The rapid development of computer science has expanded the application of numerical methods in many fields, such as the study of local scour phenomena, due to its advantages such as high accuracy, low cost and scale independence of modelling [18]. Many numerical models have been developed recently to simulate the 3D flow field and the morphological changes of the bed around circular piers.

Olsen and Melaaen [19] were among the first to predict local scour development processes by combining the three-dimensional flow field with a sediment transport model around a circular pier. The work was limited to the initial stage of scour, whereas the entire scour process was considered by Olsen and Kjellesvig [20], where good qualitative and quantitative agreement with experimentally measured scour patterns was achieved. Study [21] performed three-dimensional simulations of the flow around a circular pier with fixed scour holes in the intermediate and equilibrium phases using FLOW3D software. They found that the FLOW3D hydrodynamic model accurately modelled the complex flow patterns around the pier by comparing the numerical results with the experimental data from Melville and Raudkivi [8].

Using the CCH3D programme, Wang and Jia [22] simulated the temporal evolution of the scour hole around a bridge pier and examined various flow effects on sediment transport. Change et al. [23] performed three-dimensional calculations of the flow around a bridge pier with a fixed bed and no scour using a Large-Eddy Simulation (LES) model. In Tseng et al. [24], simulation runs were performed to investigate various properties of the three-dimensional flow around both circular and square piers subjected to a steady current by the LES model. Their model results were validated against the experimental results of Dargahi [6]. Despite the discussion of the influence of flow patterns in the scour process, no scour simulation was carried out.

Chen [25] used the RANS equations to predict scour in an array of piers in a side-by-side arrangement. The bed material was cohesive and the scour rate was assumed to vary linearly with the bed shear stress. Later, Roulund et al. [26] developed an experimental and numerical study of flow and scour around a circular pier using a k-ω turbulence model. The authors paid particular attention to horseshoe and lee–wake vortices and to the influence of boundary layer thickness, Reynolds number and bed roughness on these mechanisms. Roulund et al. [26] also derived a non-cohesive sediment model and obtained equilibrium scour depths 30% greater than the experimental data.

Khosronejad et al. [27] simulated the processes of clear water scour around piers of cylindrical, square and diamond cross-section geometries using a transient RANS k-ω model and a sediment transport model. The simulated results were compared with the experimental data. The maximum scour depths for the cylindrical and square piers were underestimated; the calculated scour was only in good agreement with that of the diamond pier. A 3D k-ϵ turbulence model and a bedload model were used by Baranya et al. [28]

to simulate the scour hole formation of several circular piers. Using a 3D hydrodynamic model incorporating a k-ω turbulence model, a sediment transport description (bed and suspended sediment) and a morphological model, Baykal et al. [29] analysed the flow and scour around a circular pier exposed to a continuous flow. Sumer [30] provides an in-depth analysis of recent developments in the numerical simulation of local scour situations.

More recently, Jia et al. [31] proposed a novel numerical method to simulate local scour around bridge piers using a 3D free-surface RANS turbulent flow model; a good agreement between simulations and experimental data was obtained. The authors found that downflow and turbulent kinetic energy around the pier are the main factors in the scouring process. Thus, the three-dimensional characterisation of the flow field and the evolution of the scour hole in the vicinity of bridge foundations using numerical modelling tools is now more feasible due to the experimental validation and the reduction in computational cost and time.

The present study aims to improve the understanding of the scour process around an oblong bridge pier embedded in a moving bed. The primary objectives are twofold: first, to characterize the time evolution of the scour depth in the vicinity of the pier, and second, to assess the quality and accuracy of the numerical approach by comparing the numerical results with experimental observations. For this investigation, the numerical simulations were performed with SSIIM, a general purpose CFD tool that solves the Navier–Stokes equations using the control volume method with the SIMPLE algorithm and the two-equation closure turbulence models [32]. The program calculates the advection–diffusion equation for sediment transport using empirical formulae for the bed boundary. For the cells closest to the water surface, the SSIIM model uses the Manning–Strickler friction coefficient, discharge and downstream water level as input values to generate the water level for the calculations using the standard backwater calculation, for which some cross-sections were considered fixed and used as reference during the simulations. The morphological model of this CFD tool is analysed here to investigate whether it accurately and effectively reproduces the complex physics governing the sediment transport processes in comparison with carefully collected laboratory data from Bento et al. [33]. The model is calibrated and validated using experimental data from Bento et al. [33].

The research paper is organised as follows. The hydrodynamic model and sediment transport equations used are described in Section 2. The experimental case study is described in Section 3, while the numerical model setup, including mesh geometric dimensions and boundary conditions, is given in Section 4. Simulations of the bed morphology and bed shear stress around the oblong bridge pier are then presented and discussed in Section 5. Finally, the main conclusions are drawn in Section 6.

2. The Hydrodynamic Model

2.1. Framework

The SSIIM model is designed for use in hydraulic/river/sediment engineering research and was developed at the Norwegian University of Science and Technology [32]. It was used in the present study because of its ability to model sediment transport and its considerable numerical stability for large time steps. Its capabilities allow long integration intervals to be computed with low computational effort, allowing the study of long time scale phenomena such as local scour. A description of the hydrodynamic model used in the current study is given here.

2.2. Flow Computation

The three-dimensional incompressible flow field of the numerical model used is calculated by the continuity and Reynolds-averaged Navier–Stokes (RANS) equations as follows (Equations (1) and (2)):

$$\frac{\partial \overline{u_i}}{\partial x_i} = 0 \tag{1}$$

$$\frac{\partial \overline{u_i}}{\partial t} + \overline{u_j}\frac{\partial \overline{u_i}}{\partial x_j} = -\frac{1}{\rho}\frac{\partial \overline{P}}{\partial x_i} + \nu_T\left(\frac{\partial^2 \overline{u_i}}{\partial x_j^2}\right) - \frac{\partial \overline{u_i' u_j'}}{\partial x_j} \quad (2)$$

where x_i and x_j (i, j = 1, 2 or 3) denote the longitudinal (x), transverse (y) and vertical (z) directions; $\overline{u_i}$ and $\overline{u_j}$ are the time-averaged velocity components; u_i' and u_j' are the corresponding fluctuation components; ρ is the water density; P is the non-hydrostatic pressure; ν is the kinematic viscosity and t is time.

The first and second terms on the left hand side of the momentum equation, Equation (2), are referred to as the transient and convective terms, respectively. On the right side, the first term is the pressure, while the second corresponds to the diffusion term. In the third term, $\overline{u_i' u_j'}$ represents the Reynolds stresses and can be calculated using the mean velocity gradients and the turbulent eddy viscosity under the Boussinesq assumption (Equation (3)):

$$-\overline{u_i' u_j'} = \nu_T\left(\frac{\partial \overline{u_i}}{\partial x_j} + \frac{\partial \overline{u_j}}{\partial x_i}\right) - \frac{2}{3}k\delta_{ij} \quad (3)$$

where δ_{ij} is the Kronecker delta (1 if $i = j$, 0 otherwise), ν_T is the turbulent viscosity and k is the turbulent kinetic energy. The last term on the right hand side of Equation (3) is included in the pressure. To calculate the eddy viscosity (ν_T), the standard k-ϵ turbulence model was used, which requires the solution of two additional equations for the transport of turbulent kinetic energy (k) and turbulent dissipation (ϵ), Equation (4) [34], where C_μ is constant and equal to 0.09.

$$\nu_T = C_\mu \frac{k^2}{\epsilon} \quad (4)$$

The criterion used to establish the convergence and numerical stability of the iterative algorithm was the reduction of all normalised residuals. This measures the local unbalance of a conserved variable in each control volume. Thus, each cell in the model has its own residual value for each of the equations being solved, which never reaches the exact value of zero. As the iteration progresses, the residuals become smaller and the variables get closer to their final solution. In addition, the solution [32] is numerically more accurate the smaller the residual value.

One of the difficulties in solving Equations (1) and (2) arises from the lack of an explicit equation for the pressure. Therefore, the Semi-Implicit Method for Pressure-Linked Equation (SIMPLE) algorithm was used for pressure coupling for all cells [35] except those closest to the water surface. For the cells closest to the surface, SSIIM calculates the water surface using a free surface algorithm, the standard 1D backwater calculation, based on a given water level point at the outlet boundary. This method is numerically stable for time increments approaching infinity, according to Hines [36], and was used in the current study.

The governing equations (Equations (1) and (2))are discretized on a structured, non-staggered grid system using the implicit finite volume approach. This strategy uses a number of techniques that differ in the way they determine the concentration on a cell surface [19]. The two most commonly used are the power-law scheme (POW) and the Second-Order Upstream scheme (SOU). Further descriptions of these schemes can be found in [37–40]. The power-law scheme (POW) is a first-order upstream scheme that converges easily; however, its results can be severely degraded by false diffusion. False diffusion can result either from the adoption of an inappropriate discretisation scheme for the convective terms in the Navier–Stokes Equations (Equation (2)) or from an inappropriate grid mesh. For the present case, the SOU scheme was used for the velocity equations, while a POW scheme was adopted for the turbulence formulations. In fact, stability problems occurred in different simulation runs when a scheme other than the first-order power-law (POW) was applied to the turbulence equations.

2.3. Sediment Transport Equations

Exner [41,42] originally proposed the sediment continuity equation, which represents the conservation of mass between sediment in a channel bed and material transported either along the bed (bed load) or in suspension (suspended load). The integration of Exner's equation over water depth is given by (Equation (5)):

$$(1-\lambda)\frac{\partial z_b}{\partial t}+\frac{\partial q_{tx}}{\partial x}+\frac{\partial q_{ty}}{\partial y}=0 \tag{5}$$

where z_b is the bed level, λ is the porosity of the bed material, and q_{tx} and q_{ty} are the total (bed and suspended) fluxes in the flow and transverse directions, respectively.

The suspended load discharge results from two main transport processes that develop through the walls of the finite volume: convection and diffusion of sediments. The combination of these two processes for steady sediment transport is given by the convection–diffusion equation (Equation (6)). The variable c represents the sediment concentration, w_s the sediment particle fall velocity and Γ_T the diffusion coefficient.

$$u_j\frac{\partial c}{\partial x_j}+w_s\frac{\partial c}{\partial z}=\frac{\partial}{\partial x_j}\left(\Gamma_T\frac{\partial c}{\partial x_j}\right) \tag{6}$$

The first term on the left hand side of Equation (6) represents sediment convection, which is the fraction of sediment transported by the average velocity component of the water over time. The transport due to the sediment fall velocity (w_s) (second term on the left side of Equation (6)) is discretised as an additional convective term and added to the velocities in the vertical direction, z [38]. The diffusion of sediments caused by turbulent mixing and concentration gradients is represented on the right side of Equation (6). The diffusion coefficient ($Gamma_T$) is typically used to simulate the turbulent mixing process. This coefficient is set equal to the eddy viscosity (ν_T) taken from the k-ϵ turbulence model. For the grid cells closest to the bed, Equation (6) is not solved, so the sediment continuity equation is typically not satisfied. The simulation of the interaction between the sediment moving towards the bed and the sediment carrying it in suspension is made possible by using the continuity discrepancy to calculate changes in bed level. It is therefore necessary to define an equilibrium concentration in the near-bed cells; Van Rijn [43] proposed an equilibrium concentration formula (Equation (7)) which is used in the current model.

$$C_{bed}=0.015\frac{D_{50}^{0.3}}{a}\frac{\left[\frac{\tau-\tau_c}{\tau_c}\right]^{1.5}}{\left[\frac{(\rho_s-\rho)g}{\rho\nu^2}\right]^{0.1}} \tag{7}$$

The variable C_{bed} is the equilibrium concentration at the bed, a is the distance from the concentration point to the bed, ν is the kinematic viscosity of the water, ρ_s is the sediment density and g is the acceleration due to gravity. The critical bed shear stress (τ_c) for sediment particle motion is obtained from the Shields curve [44] and then internally multiplied by the reduction factor (r) derived by Brooks [45] to account for the sloping bed (Equation (8)).

$$r=\frac{-\sin\varphi_s\sin\alpha_b}{\tan\theta_s}+\sqrt{\left(\frac{\sin\varphi_s\sin\alpha_b}{\tan\theta_s}\right)^2-\cos^2\varphi_s\left[1-\left(\frac{\tan\varphi_s}{\tan\theta_s}\right)^2\right]} \tag{8}$$

$alpha_b$ is the angle between the flow direction and a line perpendicular to the bed plane, $varphi_s$ is the slope angle and $theta_s$ is the slope parameter. The effective critical shear stress for a sediment particle is derived by multiplying the reduction factor (r) by the critical shear stress for a horizontal surface [32].

3. Local Scouring Experimental Data

The hydrodynamic model was calibrated and validated using the results of an experimental test carried out by Bento et al. [33]. The local scouring experiment was carried out in a 40.7 m long, 2.0 m wide and 1.0 m deep tilting flume located at the experimental facilities of the National Laboratory of Civil Engineering (LNEC) in Lisbon, Portugal.

The flow was regulated to a constant value by the speed of the associated pump and monitored by an electromagnetic flowmeter (with an accuracy of ±0.25%). The water depth in the tipping flume was controlled by two sluice gates, one at the upstream and the other at the downstream end of the flume, and monitored by two resistive probes at a sampling frequency of 25 Hz. The bed material was a uniform quartz sand with a mean grain size diameter, D_{50}, of 0.86 mm and a sediment diameter standard deviation, σ_D, of 1.28. An oblong bridge pier model, 0.11 m wide and 0.433 m long, was placed vertically in the working section on the centre plane of the flume at ≈11 m from the flume entrance. The scour experiment was stopped at the time required to attain 90% of the equilibrium scour depth (t_{90}, as stated by Sheppard et al. [46]), after 5.9 days. A value of 65.51% was obtained for the maximum bed-hole slope, corresponding to an angle of 33.23°. The hydraulic and scour conditions under which the experiment was developed are summarised in Table 1. Pointwise measurements of scour depth time evolution (d_s) at 0.03 m from the pier face were considered for calibration and validation purposes, with an accuracy of ±0.05 mm. Further details on the uncertainties associated with the experimental procedures and measurements can be found in Bento [47] and Bento et al. [33].

Table 1. Hydraulic variables of the local scouring experiment.

	Q ($\mathbf{m^3 s^{-1}}$)	h (m)	V ($\mathbf{ms^{-1}}$)	If (−)	Fr (−)	Re (−)	Re_D (−)
Experiment	0.0923	0.1440	0.3205	1.0295	0.2696	46,150	35,253.47

4. Numerical Model Setup

4.1. Mesh Geometrical Dimensions

The computational domain is commonly described as the region in 3D (or 2D) space in which the governing equations are solved by the SSIIM tool. The mesh is the result of the division of the computational domain into cells where numerical equations are solved. In this study, the computational domains in 2D (plane xy) were divided into different zones to generate non-orthogonal grid lines, and the grid points were generated using the elliptical grid generation method [48]. Only the elliptical grid was considered here, as it gave better results than the algebraic grid system, as stated by Alemi and Maia [49]. The elliptic mesh was generated by a specially developed Fortran code, which was then imported into the SSIIM software (version 47).

In order to generate a three-dimensional structured grid, different mesh sizes were tested. A 4.1 m long and 2.0 m wide computational domain (corresponding to 37W and 18W, where W is the width of the pier in meters) was chosen, resulting in 189 and 122 computational cells in the x and y directions, respectively. The vertical distribution of the grid points (z direction) was predefined in the numerical model as a percentage of the flow depth (given in Table 1). During the SSIIM computations, the grid points in the x-y plane were fixed, while those in the z direction varied according to the flow depth. The pier definition was performed by excluding the cells where the pier was located, at a distance of 1.1 m (≈10W) from the inlet boundary.

Figure 1 shows the plan view of the mesh around the oblong pier. As seen in Figure 1, the origin of the Cartesian coordinate system was at the left lateral border of the rectangular pier. The mesh is finer at the pier and bed surface and grows increasingly coarser as one moves away. The spatial increase in grid cell size was accomplished with an expansion ratio of approximately 1.01, taking into account that the grid should not be too coarse where vortices are likely to form.

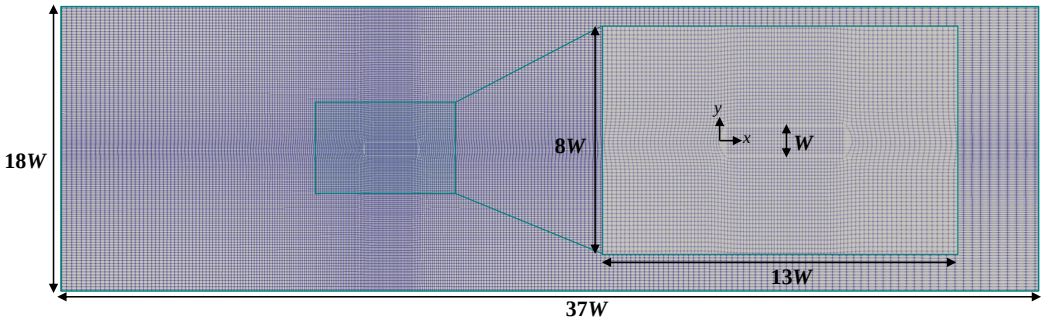

Figure 1. Plan view of the full and local grid meshes around the oblong bridge pier.

4.2. Boundary Conditions and Input Parameters

Another essential step in the numerical simulation process is the designation of appropriate boundary and input parameters, which are also the most error prone. The computational domain of the numerical simulation was divided into seven different boundaries: inlet, outlet, water surface, wall, bottom, front and back. Specific boundary conditions for the hydrodynamic model (Equation (1) to Equation (8)) were applied to these boundaries.

At the inlet, Dirichlet boundary conditions must be specified [50]. This is relatively straightforward for velocities, although it is generally more difficult to specify for turbulence. Nevertheless, Olsen [38] outlined a procedure where k and ϵ are specified based on investigations of the magnitude [51] and vertical distribution profile [52] of eddy viscosity in rivers. Given the velocity, it is also possible to estimate the shear stress at the entrance bed. It is also possible to calculate the shear stress at the inflow bed using the velocity. Equation (9) then calculates the turbulent kinetic energy (k) at the inflow bed based on the balance between turbulence production and dissipation at the bed cell.

$$k = \frac{\tau}{\rho\sqrt{C_\mu}} \tag{9}$$

Boundary conditions of zero gradient were applied to all variables at the outlet. The discharge and water depth were defined here and used to generate the water surface for the calculations in all domains using a standard backward calculation. The water surface position is determined by extrapolating the pressure from the inner cells to the surface of the water. The top grid line is affected by the vertical movement of the water surface. In accordance with their relative distance from the water's surface, the grid points below the surface are also shifted vertically. At the water surface, zero gradient boundary conditions were considered for turbulent dissipation (ϵ), while the turbulent kinetic energy (k) was assumed to be zero.

The flux through the wall, bottom, front and back is zero, i.e., the no-slip condition was imposed. Despite this, the velocity gradient towards the wall is steep and a large number of grid cells would be required to effectively resolve the gradient. Alternatively, the empirical velocity wall formula for rough boundaries [53] was used, transformed by integration over the nearest cell to the bed (Equation (10)):

$$\frac{U}{u_*} = \frac{1}{K}\ln\left(\frac{30y_w}{k_s}\right) \tag{10}$$

where u_* is the shear velocity (given by $u_* = \sqrt{\frac{\tau}{\rho}}$), K is the Von Kármán constant (equal to 0.41), y_w is the distance from the wall to the centre of the cell, k_s is the roughness height, usually calculated based on the mean particle diameter of the bed, D_{50}, and τ is the local bed shear stress. The logarithmic wall law is considered both for velocity and turbulence parameters. The turbulent kinetic energy (k) is assumed to be equal to its dissipation (ϵ) near the wall, according to Rodi's formulae [54].

The input parameters were set to values assumed in the experiments carried out. These included mean approach flow discharge and flow depth at the downstream boundary of the computational domain ("outlet" side), mean grain size diameter, density, angle of repose, fall velocity and critical bed shear stress. The angle of repose was assumed to be equal to the experimentally obtained [33]. The fall velocity was calculated using the formula in Hoffmans and Verheij [7], and the critical bed shear stress was determined using the Shields–Rouse equation [55].

5. Results and Discussion

5.1. General Considerations

Before starting the simulation case of scour development around an oblong bridge pier model, a proper calibration of the presented numerical model was performed. This process mainly required the definition of the time step and the bed roughness height.

Bearing in mind that small time steps give more accurate results but also require more computational time to reach the stability condition, a balance was made between the accuracy of the results and the required simulation time (up to t = 480 min). The SSIIM model is numerically stable for long time steps, as noted above [19,36]; numerical simulations were performed using a 5-s time step. Once selected, two different values for the bed roughness height were considered, namely $k_s = 3D_{50}$ and $k_s = 3D_{90}$. The agreement between experimental measurements and model results of the scour depth at 0.03 m from the pier face was used as the main calibration criterion. The bed roughness height parameter is the main parameter responsible for the uncertainties involved in the empirical formulae relating it to the grain size distribution. Thus, in line with Figure 2, a bed roughness height of 0.0051 m (in the present case $k_s = 3D_{90}$) was chosen, confirming the relationship proposed by Van Rijn [56].

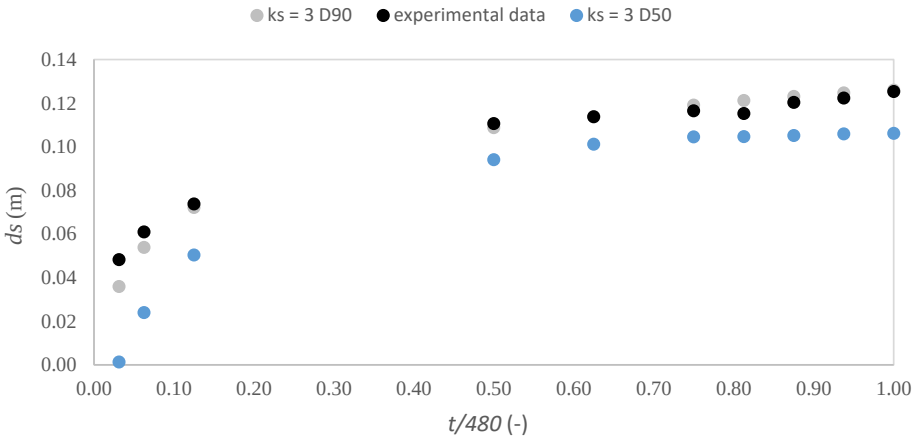

Figure 2. Calibration of the bed roughness height.

In the current study, the results of the numerical approach included the characterization of the full geometry of the bed morphology during the scouring process, as well as the bed shear stress in the vicinity of the oblong bridge pier up to t = 480 min. Numerical simulations were completed in a reasonable Central Process Unit (CPU) time. A parallel approach using 16 processors resulted in a CPU time of approximately 36 h. The results of this study were compared with experimental data from Bento et al. [33].

5.2. Scour Depth Estimates

Figure 3 presents the time evolution of the simulated and measured scour depth at 0.03 m from the pier front (relative to the time duration of t = 480 min).

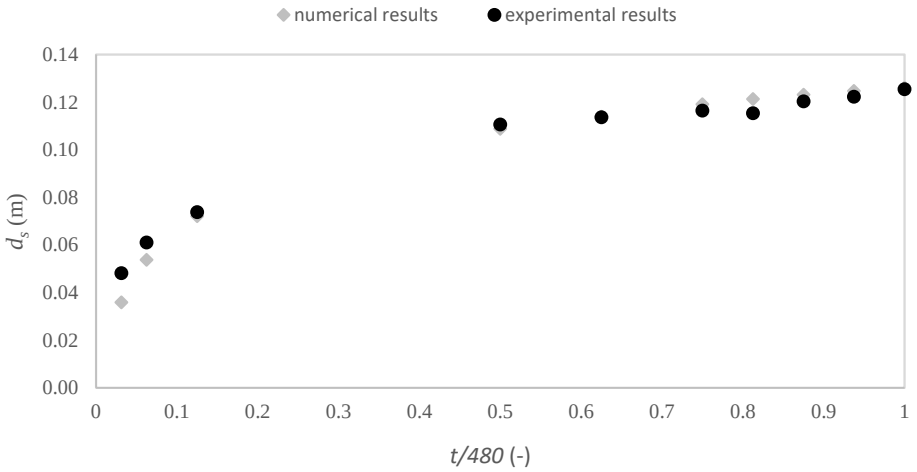

Figure 3. Experimental and computed scour depths.

The quantification of the deviation between the predicted and obtained experimental scour depth at 0.03 m from the pier front was assessed by performing a characterization of the relative errors, determined by Equation (11):

$$e_i = \frac{|d_{s,computed} - d_{s,measured}|}{d_{s,measured}} \quad (11)$$

where $d_{s,measured}$ is the experimentally measured scour depth along each scour bed profile, and $d_{s,computed}$ is the scour depth computed by the numerical model. Table 2 gives these scour depths and their relative errors.

Table 2. Scour depth relative error (e_i), determined by Equation (11).

t (min)	$d_{s,measured}$ (m)	$d_{s,computed}$ (m)	e_i (%)
15	0.048	0.036	25.4
30	0.061	0.054	11.8
60	0.074	0.072	2.2
240	0.111	0.109	1.7
300	0.114	0.114	−0.2
360	0.117	0.119	−2.3
390	0.115	0.121	−5.2
420	0.120	0.123	−2.4
450	0.122	0.125	−2.0
480	0.125	0.126	−0.5

The simulated scour depth evolution ($d_{s,computed}$) started a little later than the experimentally observed one ($d_{s,measured}$). It may be the result of the simulated horseshoe vortex or turbulent fluctuations at the beginning, which are relatively weaker than the experimental fluctuations. According to Table 2, the numerical model shows an underprediction of more than 25% for t = 15 min, which decreases significantly to 2.2% for t = 60 min and 1.7% for t = 240 min. From t = 300 to t = 480 min, the numerical model overpredicts the experimental data by percentages ranging from 0.2% to 5.2%. It can therefore be concluded that the numerical model predicts the measured scour depths with significant accuracy (with an average relative error of 2.9%).

5.3. Bed Morphology

Figure 4 shows the computed bed morphology in the vicinity of the long bridge pier at different times of the local scour experiment, from t = 15 min to t = 480 min. The zero point in the vertical plane (z) corresponds to the bed level before scouring. The results provide

an overview of the detailed scour and deposition processes occurring around an oblong bridge pier laboratory model that have been triggered by turbulent flow dynamics.

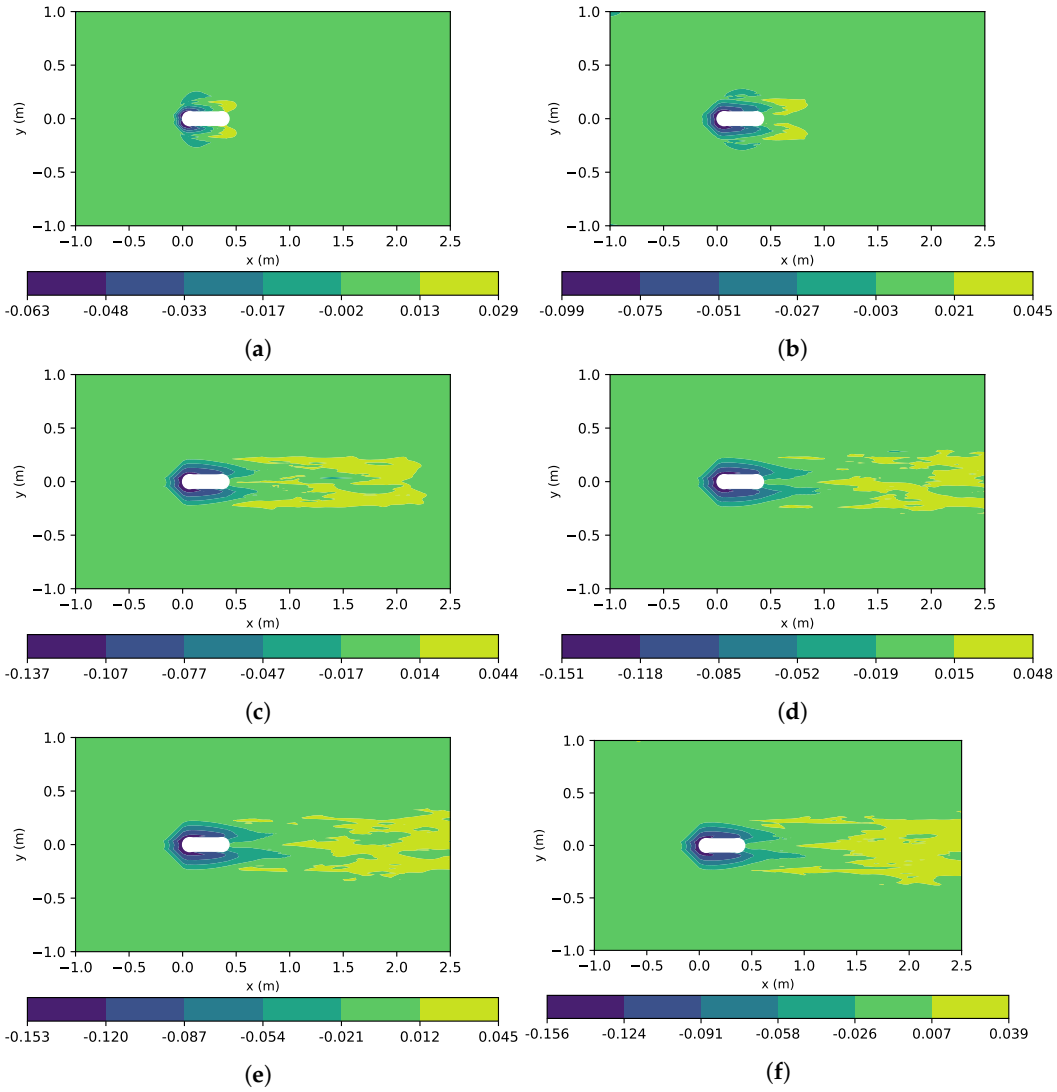

Figure 4. Scour hole and deposition region around the oblong bridge pier (dimensions in meters). (**a**) t = 15 min. (**b**) t = 60 min. (**c**) t = 240 min. (**d**) t = 360 min. (**e**) t = 420 min. (**f**) t = 480 min.

Sediment bed transport started at the sides of the pier due to the higher bed shear stress there (still noticeable for t = 15 min, Figure 4a). In later stages of the process, scour develops both along the lateral sides and upstream, which is indicative of the dominance of the horseshoe vortex system (see Figure 4b). From t = 60 (Figure 4b) to t = 480 min (Figure 4f), the simulation showed a steady increase in bed scour in the vicinity of the 0.11 m wide pier, suggesting that the acceleration effect, coupled with the horseshoe vortices, contributed significantly to sediment entrainment. Sediment transported from the vicinity of the pier was deposited downstream as a result of periodic shedding of vortices in the wake region. According to the numerical model results, the scour hole contours and the location of the maximum scour area on the upstream side of the pier agreed well with the experimental results [33].

A better understanding of the scour process was obtained by examining different azimuthal planes of the scour bed profiles around the oblong bridge pier. Figure 5 shows the numerical results of the bed profiles over time (for the above mentioned times) on the longitudinal median plane (Figure 5a) and on the plane perpendicular to the flow direction (Figure 5b).

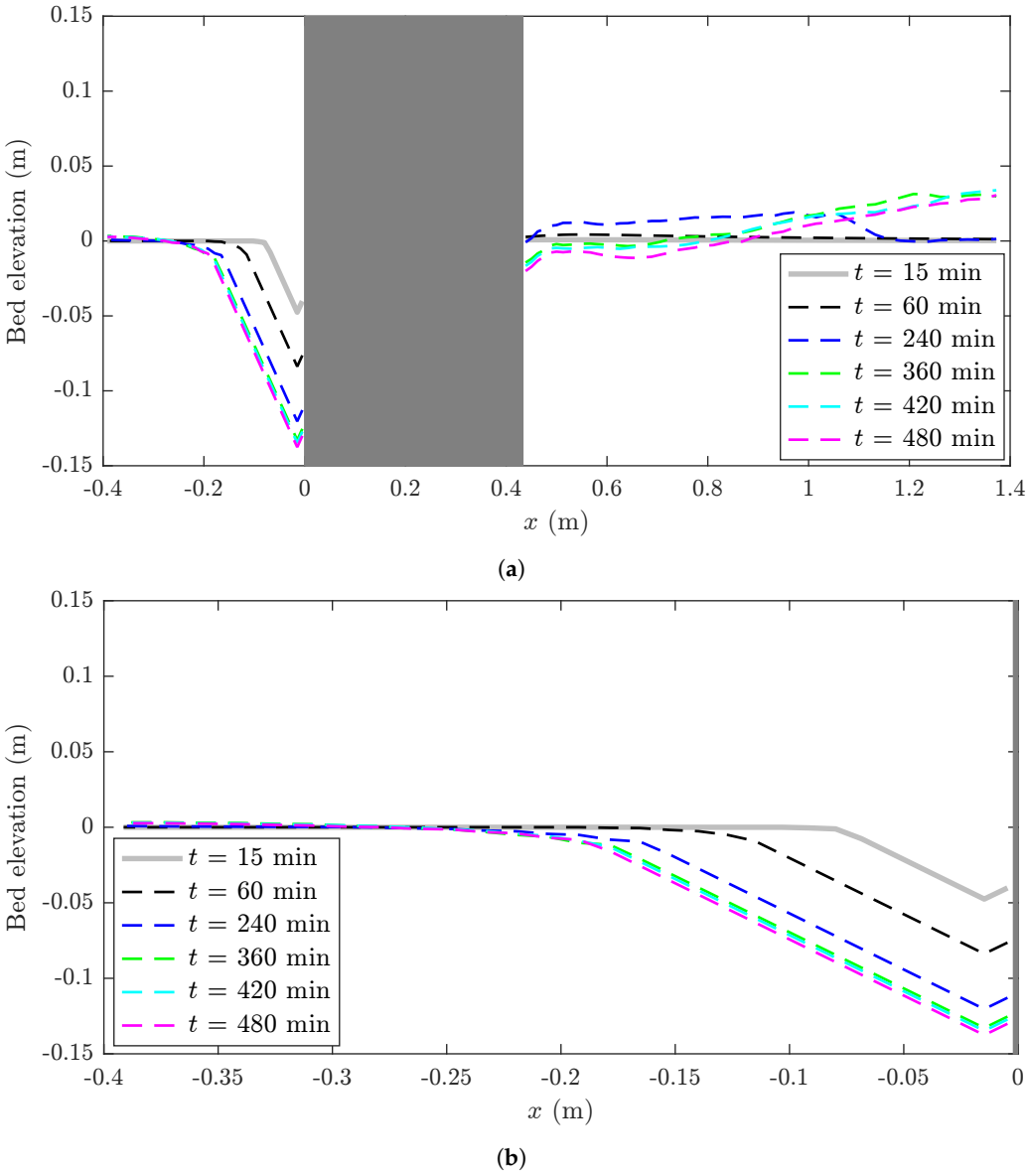

Figure 5. Scoured bed hole profiles on the longitudinal mid-plane (**a**) and on the plane normal to the flow direction (**b**). Flow direction: x-axis.(**a**) At the pier's longitudinal mid-plane. (**b**) At the plane normal to flow direction.

The rate of growth of the scour hole has slowed down over time. The width of the scour hole upstream of the pier ranges between 0.73W (t = 15 min) and 2.5W (t = 480 min), as can be seen in Figure 5a. The maximum scour depth was observed along the mid-plane of the oblong pier model, a relevant parameter for stability analysis of bridge foundations, and was confirmed to occur at a distance of 0.015 m from the pier face (equivalent to a distance of 0.14W).

Taking into account the upstream scoured hole profile at the pier centre plane, the maximum bed-hole slope value was calculated for each of the analysed time instants (t = 15, 60, 240, 360, 420 and 480 min). These values were then compared with the angle of repose of the sediment bed material and the value obtained for the end of the scouring experiment [33]. The slope of the upstream scoured bed profile for t = 480 min was equal to 36.61°, 9% greater than the angle of repose obtained for the end of the local scouring experiment (as indicated in Bento et al. [33]). The angles were approximately 10% and 18% higher than the classical 30° repose angle value for wet sand [57] for t = 5.9 days and t = 480 min, respectively.

5.4. Bed Shear Stress

Contours of the normalized mean bed shear stress (τ/τ_m) around the oblong bridge pier are shown in Figure 6, where τ_m is the bed shear stress of the approach flow. An initial preponderance of the normalised bed shear stress can be observed at the sides of the pier (Figure 6a), which corresponds to the scour development (shown in Figure 4a). For the remaining times, up to t = 480 min, an increase in τ/τ_m was obtained immediately in front of the pier, indicating higher scour depths at the front of the oblong pier (Figure 6b–f). Near the upstream edge of the scour hole (the "<" shape), the bed shear stress is lower than in the region where the horseshoe vortex system occurs, which is consistent with study [11] and references therein.

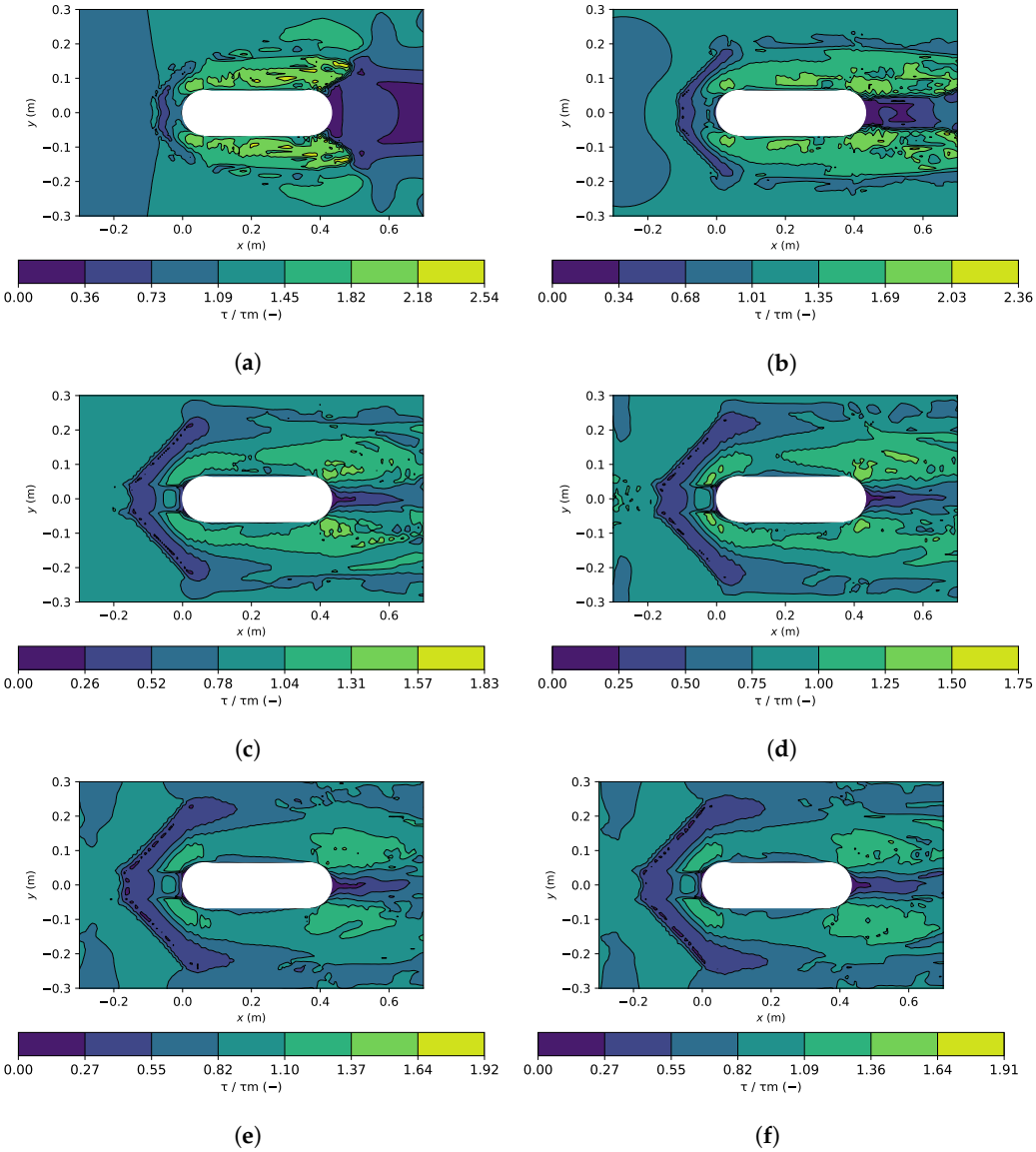

Figure 6. Normalized bed shear stress (τ/τ_m) contours around the oblong bridge pier. (**a**) t = 15 min. (**b**) t = 60 min. (**c**) t = 240 min. (**d**) t = 360 min. (**e**) t = 420 min. (**f**) t = 480 min.

6. Conclusions

Local scour results from an experimental facility were used to assess the performance of a numerical CFD model in terms of bed morphology and bed shear stress around an oblong bridge pier, and to provide information on the uncertainties associated with their prediction. The laboratory experiments carried out in conjunction with the numerical simulations

showed that the maximum scour and dynamic flow characteristics in the vicinity of the oblong bridge pier are quite similar if the numerical model is properly calibrated.

The numerical simulations were performed using the CFD tool SSIIM and were designed to provide insights into key features of the flow and scour characteristics that cannot all be obtained simultaneously when conducting a local scour experiment. For example, the assessment of time and space distributions of bed shear stress and scour holes. In the current study, a detailed investigation of the geometry of the bed morphology and bed shear stress was carried out in the vicinity of a 0.11 m wide oblong pier.

Regarding the local scour simulations, the results indicate that the SSIIM model, properly calibrated and validated with the laboratory data [33], predicted the measured scour depths with significant accuracy (with an average relative error of less than 3%) and reasonable computational times. The spatial and temporal evolution of the bed shear stress around the oblong bridge pier laboratory model, while consistent with the process of scour development, is still a subject of growing interest in both the academic and engineering communities.

Author Contributions: Conceptualization, A.M.B., J.P.P., T.V. and L.C.; methodology and design, A.M.B., J.P.P., T.V. and L.C.; formal analysis, A.M.B.; investigation, A.M.B.; writing—original draft preparation, A.M.B.; writing—review and editing, A.M.B., J.P.P., T.V. and L.C. All authors have read and agreed to the published version of the manuscript.

Funding: This research was funded by the Portuguese Foundation for Science and Technology (FCT) grant number PD/BD/127798/2016. This research was co-supported by strategical funding from FCT UIDB/04423/2020 and UIDP/04423/2020.

Institutional Review Board Statement: Not applicable.

Informed Consent Statement: Not applicable.

Data Availability Statement: The data presented in this study are available on reasonable request from the authors.

Conflicts of Interest: The authors declare no conflict of interest.

References

1. Cook, W.; Barr, P.J.; Halling, M.W. Bridge Failure Rate. *J. Perform. Constr. Facil.* **2015**, *29*, 04014080. [CrossRef]
2. Flint, M.M.; Fringer, O.; Billington, S.L.; Freyberg, D.; Diffenbaugh, N.S. Historical Analysis of Hydraulic Bridge Collapses in the Continental United States. *J. Infrastruct. Syst.* **2017**, *23*, 04017005. [CrossRef]
3. Proske, D. *Bridge Collapse Frequencies Versus Failure Probabilities*; Springer International Publishing: Berlin/Heidelberg, Germany, 2018. [CrossRef]
4. Rocha, J.S.; do Carmo, J.S.A.; Lemos, L.J.L.; da Silva, V.D.; da Silva Rebelo, C.A. Pontes construídas sobre fundos aluvionares: O colapso da ponte Hintze Ribeiro. *Recur. Hidricos* **2008**, *29*, 41–57.
5. Chiew, Y.M.; Lai, J.S.; Link, O. Experimental, Numerical and Field Approaches to Scour Research. *Water* **2020**, *12*, 1749. [CrossRef]
6. Dargahi, B. The turbulent flow field around a circular cylinder. *Exp. Fluids* **1989**, *8*, 1–12. [CrossRef]
7. Hoffmans, G.; Verheij, H. *Scour Manual*; A.A. Balkema/CRC Press: Rotterdam, The Netherlands, 1997; Volume 96
8. Melville, B.W.; Raudkivi, A.J. Flow characteristics in local scour at bridge piers. *J. Hydraul. Res.* **1977**, *15*, 373–380. [CrossRef]
9. Graf, W.; Istiarto, I. Flow pattern in the scour hole around a cylinder. *J. Hydraul. Res.* **2002**, *40*, 13–20. [CrossRef]
10. Unger, J.; Hager, W.H. Down-flow and horseshoe vortex characteristics of sediment embedded bridge piers. *Exp. Fluids* **2006**, *42*, 1–19. [CrossRef]
11. Kirkil, G.; Constantinescu, S.G.; Ettema, R. Coherent Structures in the Flow Field around a Circular Cylinder with Scour Hole. *J. Hydraul. Eng.* **2008**, *134*, 572–587. .:5(572). [CrossRef]
12. Diab, R.M.A.E.A. Experimental Investigation on Scouring Around Piers of Different Shape and Alignment in Gravel. Ph.D. Thesis, TU Darmstadt, Darmstadt, Germany, 2011.
13. Bento, A.M.; Viseu, T.; Pêgo, J.P.; Couto, L. Experimental Characterization of the Flow Field around Oblong Bridge Piers. *Fluids* **2021**, *6*, 370. [CrossRef]
14. Escauriaza, C.; Paola, C.; Voller, V.R. Computational Models of Flow, Sediment Transport and Morphodynamics in Rivers. In *Gravel-Bed Rivers*; John Wiley & Sons, Ltd.: Hoboken, NJ, USA, 2017; pp. 1–31. [CrossRef]
15. Briley, W.R.; McDonald, H. Computation of three-dimensional horseshoe vortex flow using the Navier-Stokes equations. In Proceedings of the Seventh International Conference on Numerical Methods in Fluid Dynamics, Stanford, CA, USA, 23–27 June 1980; Springer: Berlin/Heidelberg, Germany, 1981; pp. 91–98. [CrossRef]

16. Kwak, D.; Rogers, S.E.; Kaul, U.K.; Chang, J.L.C. A numerical study of incompressible juncture flows. In Proceedings of the Tenth International Conference on Numerical Methods in Fluid Dynamics, Beijing, China, 23–27 June 1986; Springer: Berlin/Heidelberg, Germany, 1986; pp. 398–402. [CrossRef]
17. Deng, G.B.; Piquet, J. Navier-Stokes computations of horseshoe vortex flows. *Int. J. Numer. Methods Fluids* **1992**, *15*, 99–124. [CrossRef]
18. Zhang, Q.; Zhou, X.L.; Wang, J.H. Numerical investigation of local scour around three adjacent piles with different arrangements under current. *Ocean Eng.* **2017**, *142*, 625–638. [CrossRef]
19. Olsen, N.R.B.; Melaaen, M.C. Three-Dimensional Calculation of Scour Around Cylinders. *J. Hydraul. Eng.* **1993**, *119*, 1048–1054. .:9(1048). [CrossRef]
20. Olsen, N.R.B.; Kjellesvig, H.M. Three-dimensional numerical flow modeling for estimation of maximum local scour depth. *J. Hydraul. Res.* **1998**, *36*, 579–590. [CrossRef]
21. Richardson, J.E.; Panchang, V.G. Three-Dimensional Simulation of Scour-Inducing Flow at Bridge Piers. *J. Hydraul. Eng.* **1998**, *124*, 530–540. .:5(530). [CrossRef]
22. Wang, S.; Jia, Y. Computational simulations of local scour at bridge crossings-Capabilities and limitations. In Proceedings of the Proceedings ASCE International Water Resources Engineering Conference: Past Accomplishments and New Challenges" ASCE, Seattle, WA, USA, 8–12 August 1999.
23. Chang, W.Y.; Lai, J.S.; Yen, C.L. Simulation of scour depth evolution at pier nose. In Proceedings of the 1999 International Water Resources Engineering Conference, Seattle, WA, USA, 8–12 August 1999; Session BS–05; Water Resources Publications LLC: Highlands Ranch, CO, USA, 1999.
24. Tseng, M.H.; Yen, C.L.; Song, C.C.S. Computation of three-dimensional flow around square and circular piers. *Int. J. Numer. Methods Fluids* **2000**, *34*, 207–227. .:3<207::aid-fld31>3.0.co;2-r. [CrossRef]
25. Chen, H. Numerical simulation of scour around complex piers in cohesive soil. In Proceedings of the First International Conference on Scour of Foundations International Society of Soil Mech and Foundations, College Station, TX, USA, 17–20 November 2002.
26. Roulund, A.; Sumer, B.M.; Fredsøe, J.; Michelsen, J. Numerical and experimental investigation of flow and scour around a circular pile. *J. Fluid Mech.* **2005**, *534*, 351–401. [CrossRef]
27. Khosronejad, A.; Kang, S.; Sotiropoulos, F. Experimental and computational investigation of local scour around bridge piers. *Adv. Water Resour.* **2012**, *37*, 73–85. [CrossRef]
28. Baranya, S.; Olsen, N.R.B.; Stoesser, T.; Sturm, T. Three-Dimensional RANS Modeling of Flow Around Circular Piers using Nested Grids. *Eng. Appl. Comput. Fluid Mech.* **2012**, *6*, 648–662.
29. Baykal, C.; Sumer, B.M.; Fuhrman, D.R.; Jacobsen, N.G.; Fredsøe, J. Numerical investigation of flow and scour around a vertical circular cylinder. *Philos. Trans. R. Soc. A Math. Phys. Eng. Sci.* **2015**, *373*, 20140104. [CrossRef]
30. Sumer, B. A review of recent advances in numerical modelling of local scour problems. In Proceedings of the Fifth International Conference on Scour and Erosion, San Francisco, CA, USA, 7–10 November 2010; CRC Press: Boca Raton, FL, USA, 2015; pp. 61–70. [CrossRef]
31. Jia, Y.; Altinakar, M.; Guney, M.S. Three-dimensional numerical simulations of local scouring around bridge piers. *J. Hydraul. Res.* **2017**, *56*, 351–366. [CrossRef]
32. Olsen, N. *A Three-Dimensional Numerical Model for Simulation of Sediment Movements in Water Intakes with Moving Option—User's Manual*; The Norwegian University of Science and Technology: Trondheim, Norway, 2018.
33. Bento, A.M.; Couto, L.; Viseu, T.; Pêgo, J.P. Image-Based Techniques for the Advanced Characterization of Scour around Bridge Piers in Laboratory. *J. Hydraul. Eng.* **2022**, *148*, 06022004. [CrossRef]
34. Wilcox, D. *Turbulence Modeling for CFD*; DCW Industries, Inc.: La Cãnada, CA, USA, 2006.
35. Patankar, S.; Spalding, D. A calculation procedure for heat, mass and momentum transfer in three-dimensional parabolic flows. *Int. J. Heat Mass Transf.* **1972**, *15*, 1787–1806. [CrossRef]
36. Hines, Jonathan. A Comparative Study of the SIMPLE and Fractional Step Time Integration Methods for Transient Incompressible Flows. Master's Thesis, University of Waterloo, Waterloo, ON, USA, 2008.
37. Patankar, S. *Numerical Heat Transfer and Fluid Flow*; Hemisphere Pub. Corp. McGraw-Hill: New York, NY, USA, 1980; p. 197.
38. Olsen, N. A Three-Dimensional Numerical Model for Simulation of Sediment Movements in Water Intakes. Ph.D. Thesis, Norwegian Institute of Technology, University of Trondhein, Trondheim, Norway, 1991.
39. Melaaen, M.C. Calculation of fluid flows with staggered and nonstaggered curvilinear nonorthogonal grids-the theory. *Numer. Heat Transf. Part B Fundam.* **1992**, *21*, 1–19. [CrossRef]
40. Versteeg, H.K. *An Introduction to Computational Fluid Dynamics: The Finite Volume Method*; Pearson Education Ltd.: Harlow, UK; New York, NY, USA, 2007.
41. Exner, F. Zur physik der dunen. *Akad. Wiss. Wien Math. Naturwiss. Kl.* **1920**, *129*, 929–952. (In German)
42. Exner, F.M. Uber die wechselwirkung zwischen wasser und geschiebe in flussen. *Akad. Wiss. Wien Math. Naturwiss. Kl.* **1925**, *134*, 165–204.
43. Rijn, L.C.V. Sediment Transport, Part III: Bed forms and Alluvial Roughness. *J. Hydraul. Eng.* **1984**, *110*, 1733–1754. [CrossRef]
44. Shields, A. *Application of Similarity Principles and Turbulence Research to Bed-Load Movement*; Caltech Library: Pasadena, CA, USA, 1936.

45. Brooks, N.H. Discussion on "Boundary shear stresses in curved trapezoidal channels". *J. Hydraul. Div. ASCE* **1963**, *89*, 327–333. [CrossRef]
46. Sheppard, D.M.; Demir, H.; Melville, B.W. *Scour at Wide Piers and Long Skewed Piers*; Transportation Research Board: Washington, DC, USA, 2011; Volume 682. [CrossRef]
47. Bento, A.M. Risk-Based Analysis of Bridge Scour Prediction. Ph.D. Thesis, Faculty of Engineeing of the University of Porto, Porto, Portugal, 2021.
48. Thompson, J.F. Elliptic grid generation. *Appl. Math. Comput.* **1982**, *10–11*, 79–105. [CrossRef]
49. Alemi, M.; Maia, R. Numerical Simulation of the Flow and Local Scour Process around Single and Complex Bridge Piers. *Int. J. Civ. Eng.* **2016**, *16*, 475–487. [CrossRef]
50. Olsen, N.R.B. *Numerical Modelling and Hydraulics*; Technical Report; Norwegian University of Science and Technology: Trondheim, Norway, 2012.
51. Keefer, T.N. *The Relation of Turbulence to Diffusion in Open-Channel Flows*; US Department of the Interior, Geological Survey, Water Resources Division: Reston, VA, USA, 1971.
52. Naas, S.L. Flow Behavior in Alluvial Channel Bends. Ph.D. Thesis, Colorado State University, Fort Collins, CO, USA, 1977.
53. Schlichting, H.; Gersten, K. *Boundary-Layer Theory*; Springer: Berlin/Heidelberg, Germany, 2017. [CrossRef]
54. Rodi, W. *Turbulence Models and Their Application in Hydraulics: A State-of-the Art Review*; A.A. Balkema: Rotterdam, The Netherlands; Broofield, VT, USA, 1993.
55. Guo, J. Hunter Rouse and Shields diagram. In *Advances in Hydraulics and Water Engineering*; World Scientific Publishing Company: Singapore, 2002. [CrossRef]
56. Van Rijn, L.C. *Principles of Sediment Transport in Rivers, Estuaries, and Coastal Seas*; Aqua Publications: Amsterdam, The Netherlands, 1993; Volume 1006
57. Matos Fernandes, M. *Mecânica dos Solos—Conceitos e Princípios Fundamentais*; Oficina de Textos: São Paulo, Brazil, 2016; Volume 1.